


Cite this: *Nanoscale*, 2023, **15**, 19407

# Sonocatalytic cancer therapy: theories, advanced catalysts and system design

Ruiyan Li,<sup>†a</sup> Xuan Wang,<sup>†a</sup> Jiacheng Shi,<sup>a</sup> Yong Kang<sup>\*a</sup> and Xiaoyuan Ji <sup>\*a,b</sup>

Treating cancer remains one of the most formidable challenges in modern medicine, with traditional treatment options often being limited by poor therapeutic outcomes and unacceptable side effects. Nanocatalytic therapy activates tumor-localized catalytic reactions *in situ* via nontoxic or minimally toxic nanocatalysts responding to unique cues from the tumor microenvironment or external stimuli. In particular, sonocatalytic cancer therapy is a promising approach that has emerged as a potential solution to this problem through the combination of ultrasound waves and catalytic materials to selectively target and destroy cancer cells. Compared to light, ultrasound exhibits higher spatial precision, lower energy attenuation, and superior tissue penetrability, furnishing more energy to catalysts. Multidimensional modulation of nanocatalyst structures and properties is pivotal to maximizing catalytic efficiency given constraints in external stimulative energy as well as substrate types and levels. In this review, we discuss the various theories and mechanisms underlying sonocatalytic cancer therapy, as well as advanced catalysts that have been developed for this application. Additionally, we explore the design of sonocatalytic cancer therapy systems, including the use of heterojunction catalysts and the optimal conditions for achieving maximum therapeutic effects. Finally, we highlight the potential benefits of sonocatalytic cancer therapy over traditional cancer treatments, including its noninvasive nature and lower toxicity.

Received 7th September 2023,  
Accepted 2nd November 2023

DOI: 10.1039/d3nr04505f

rsc.li/nanoscale

## 1 Introduction

Many nanocatalysts with distinct and superior features have recently been used *in vivo* to address medical issues, offering

efficient therapeutic approaches for a variety of diseases, including cancer, bacterial infection, and inflammation.<sup>1</sup> This promising new field is termed catalytic medicine. Nanocatalytic therapy utilizes nontoxic or low-toxicity nanocatalysts to initiate tumor-localized *in situ* catalytic reactions that convert substrates in the tumor microenvironment (TME) into effective therapeutic agents in response to unique cues from the TME or external stimuli. The most widely used reactions have oxygen or water as the substrate, generating reactive oxygen species (ROS) as the main products to achieve tumoricidal

<sup>a</sup>Academy of Medical Engineering and Translational Medicine, Medical College, Tianjin University, Tianjin 300072, China. E-mail: kangyong@tju.edu.cn, jixiaoyuan@tju.edu.cn

<sup>b</sup>Medical College, Linyi University, Linyi 276000, China

<sup>†</sup>These authors contributed equally to this work.



Ruiyan Li

Ruiyan Li received his B.S. degree from Tianjin Medical University in 2022, and is now pursuing her master's degree under the guidance of Prof. Xiaoyuan Ji at Tianjin University. His current research focuses on the design and development of stimulation-responsive nanobiomaterials for tumor therapy, tissue repair, biosensing and other applications.



Yong Kang

Dr Yong Kang is currently employed as an Assistant Researcher at Tianjin University. He obtained his PhD degree from the Institute of Process Engineering, Chinese Academy of Sciences, in 2021. His primary research focuses on the design, construction, and application of anti-tumor nanomedicine, including heterojunction nanodrugs and biomimetic micro/nano-robotic drugs.

dal oxidative damage for therapeutic purposes.<sup>2,3</sup> Concurrently, catalytic reactions can deplete GSH and glucose, amplifying oxidative stress damage and starvation therapy against cancers, respectively.<sup>4</sup> Additionally, gaseous signaling molecules produced through catalysis, such as nitric oxide (NO),<sup>5</sup> carbon monoxide (CO),<sup>6</sup> and hydrogen (H<sub>2</sub>),<sup>7</sup> have been proven to play roles in disease treatment and physiological processes.<sup>8</sup>

Catalytic therapy can be classified into two groups based on different catalytic mechanisms: externally prompted catalytic therapy and nonexternally triggered catalytic therapy. Nonexternally triggered catalytic therapy typically involves utilizing nanozymes or Fenton reagents to catalyze substrates inherent to the TME, such as abundant glucose and over-expressed hydrogen peroxide (H<sub>2</sub>O<sub>2</sub>), to generate therapeutic products or deplete substrates needed for tumor growth. Chemodynamic therapy exemplifies nonexternally triggered catalytic therapy, primarily relying on Fenton or Fenton-like reactions to decompose endogenous hydrogen peroxide to produce hydroxyl radicals (<sup>•</sup>OH).<sup>9–12</sup> Chemodynamic therapy requires no external stimulation, but the singular catalytic substrate type and limited substrate availability within tumors restrict its therapeutic efficacy. Externally triggered catalytic therapy refers to catalysts undergoing the separation of electron–hole pairs under certain external stimuli, for example, ultrasound (US), light, magnetism, and heat, and utilizing the redox potential of the separated holes or electrons to catalyze specific oxidation–reduction reactions to produce therapeutic agents for disease treatment. Owing to the synergistic effects of diverse external stimuli and catalysts, externally triggered catalytic therapy has lower constraints due to the internal microenvironment and higher catalytic efficiency and can catalyze a more versatile range of substrates.

The concept of photocatalytic therapy can be traced back to 1900,<sup>13</sup> with modern research originating in 1975 when

Dougherty *et al.* first demonstrated photocatalysis.<sup>14</sup> Since then, it has been thoroughly investigated and explored, and it is now clinically approved for the treatment of esophageal, cutaneous, and head and neck cancers.<sup>15,16</sup> However, conventional photocatalytic therapy still faces formidable challenges such as low tissue penetration depth and potential phototoxicity that are difficult to overcome. Sonocatalytic therapy overcomes this limitation, as ultrasound has higher spatial precision, lower energy attenuation, and higher biological tissue penetrability, reaching deep-seated organs inaccessible to light. Sonocatalytic therapy employs low-intensity ultrasound as an external stimulus to activate sonosensitizers, promoting cytotoxic ROS generation within cancer cells and consequently causing cancer cell apoptosis/necrosis. Specifically, the introduced ultrasound first interacts with the adjacent liquid environment to generate abundant bubbles, which then grow and burst in a process known as cavitation. Then, the enormous heat generated from cavitation can lead to pyrolysis or sonoluminescence, consequently triggering sonosensitizer-catalyzed generation of ROS from endogenous substrates (H<sub>2</sub>O and O<sub>2</sub>). Similar to photocatalytic therapy, sonocatalytic therapy consists of three fundamental elements: an ultrasound excitation source, sonosensitizers, and substrates. The active sites of sonosensitizers and the species and concentrations of therapeutically generated products are critical factors influencing sonocatalytic therapy. Therefore, multidimensional modulation of sonosensitizer structures and properties to maximize quantum yields and catalytic efficiencies under limited external stimulative energy and substrate types and levels is key to elevating the clinical potential of nanocatalytic therapies.

This review article mainly focuses on the mechanisms of sonocatalytic therapy as well as piezoelectric and heterojunction sonosensitizers. It then introduces the design and applications of traditional, piezoelectric, and heterojunction sonosensitizers used in cancer treatment in recent years (Fig. 1). This review aims to provide some insights that may contribute to the progress of sonocatalytic treatment.



**Xiaoyuan Ji**

*Prof. Xiaoyuan Ji is a full professor at Tianjin University and the deputy director of the Engineering Research Center of the Ministry of Education for Intelligent Medical Engineering. He received his PhD degree at the Institute of Process Engineering, Chinese Academy of Sciences and Harvard University. His research interest is focused on biomaterials, nanomedicine and nanobiotechnology, which involve the design, fabrication,*

*biomedical application and clinical translation of versatile biomaterials, including heterojunction nanomedicine, micro-/nanorobots, and drug/gene delivery, nanodynamic therapy, nanocatalytic therapy, and localized disease therapy agents.*

## 2 The mechanism of sonocatalytic therapy

In recent years, the mechanisms of sonocatalytic therapy have been extensively explored, but the exact mechanisms remain unresolved due to the complexity of the processes. As illustrated in Fig. 2, we have summarized the putative mechanisms of sonocatalytic therapy, including thermal effects, cavitation effects, piezoelectric effects, and sonochemical reactions.<sup>17,18</sup> Additionally, we elucidated the electron transfer mechanisms in different types of sonosensitizers.

### 2.1 Cavitation effect

Under the action of an introduced ultrasonic field, ultrasound interacts with the adjacent liquid environment to generate abundant bubbles. Then, microscopic bubbles (cavitation nuclei) existing in the liquid vibrate, grow, and continually accumulate ultra-



Fig. 1 Schematic diagram of sonocatalytic therapy.

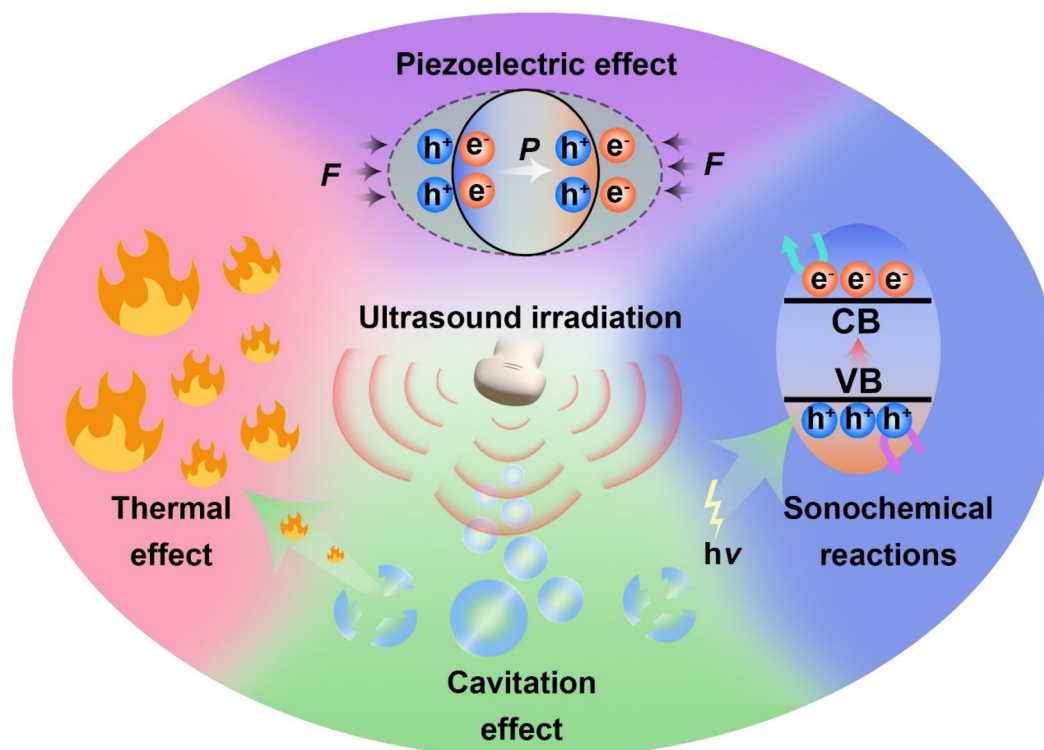


Fig. 2 Schematic illustration of mechanisms for sonocatalytic therapy.

sonic energy until the energy reaches a threshold, whereupon the cavitation bubbles implode violently. This process is termed the cavitation effect.<sup>19–21</sup> Cavitation includes inertial cavitation and stable cavitation. Inertial cavitation refers to the process of trapped bubbles in a fluid undergoing rapid expansion and violent collapse under ultrasound. In these explosive cavitation bubble events, enormous heat and pressure energies are yielded due to the conversion of mechanical energy.<sup>22</sup>

Based on the extremely high heat generated by inertial cavitation, two potential fundamental mechanisms have been proposed, sonoluminescence and pyrolysis, to account for ROS generation in sonochemical reactions.<sup>23,24</sup> Sonoluminescence refers to the emission of light produced by the implosive collapse of cavitation bubbles induced by ultrasound. Umemura and colleagues described light emission with a peak at ~450 nm generated from the interaction of ultrasound and saline solution.<sup>25</sup> Analogous to photodynamic therapy, as most sonosensitizers originate from photosensitizers, the light generated from sonoluminescence can activate sonosensitizers to produce electron–hole pairs ( $e^-h^+$ ) in an aqueous environment, subsequently triggering ROS generation. To date, the mechanism of sonoluminescence remains unclear, with many hypotheses proposed, including triboluminescence, bremsstrahlung, blackbody radiation, *etc.*<sup>26</sup> Pyrolysis is the second mechanism for ROS production. The implosive collapse of cavitation bubbles in inertial cavitation generates extremely high temperatures (up to 10 000 K) and enormous pressures (81 MPa) at the cavitation core.<sup>27</sup> Such extreme heat and pressure may decompose  $H_2O$  into free radicals ( $\cdot OH$ ), which can further react with endogenous substrates to produce other ROS. Owing to the localized energy release and high cooling rates, collateral damage to adjacent tissues is minimal.<sup>28</sup> Although putative mechanisms have been thoroughly investigated *in vivo* and *in vitro*, the complexity of ultrasonic cavitation processes prevents us from knowing the precise and reliable mechanism. Nevertheless, it is apparent that the combination of low-intensity ultrasound and sonosensitizers results in an increased production of ROS through mechanisms such as sonoluminescence or pyrolysis, hence enhancing the cytotoxic effects.

## 2.2 Thermal effect

During stable cavitation, bubbles oscillate around an equilibrium radius in the liquid and can sustain multiple acoustic compression–rarefaction cycles. Stable cavitation usually leads to microstreams in the surrounding liquid, applying shear forces to adjacent tissues.<sup>29</sup> When stable cavitation occurs in tissues, the microstreams generated by stable cavitation bubbles further cause rubbing between bubbles and tissues, accompanied by tissue oscillations. Thus, ultrasonic energy is converted into heat, elevating the tissue temperature, the well-known ultrasonic thermal effect.<sup>22</sup>

## 2.3 Piezoelectric effect

While exploring crystal symmetry in 1880, Pierre and Jacques Curie found the piezoelectric effect: materials with noncentro-

symmetric structures accumulate electric charges in response to mechanical stress.<sup>30</sup> When mechanical stresses (including tension, compression, or torsion) are applied to piezoelectric materials, microscopic mechanical deformations occur in the materials due to external forces. Lacking central symmetry, negative and positive charge centers no longer coincide, contributing to polarization.<sup>19,31–33</sup> After the generation of negatively and positively polarized charges, they migrate to opposite sides of the piezoelectric material, establishing a built-in electric field and piezoelectric potential.

## 2.4 Sonochemical reactions

The mechanism of sonosensitizer-catalyzed sonochemical reactions is that sonosensitizers absorb external stimulative energy (pyrolysis or sonoluminescence) to excite the sonosensitizers to excited states, generating electron–hole separation. The separated holes and electrons migrate to the catalyst surface to catalyze the corresponding reduction and oxidation reactions, thereby converting innocuous substrates into effective therapeutic agents at disease sites for treatment. The most commonly used therapeutic approaches at present are sonochemical reactions with ROS, which achieve treatment effects by inducing redox imbalance in cancer cells. Additionally, GSH, which maintains redox homeostasis in cancer cells, can also be catalytically depleted to indirectly enhance ROS therapeutic efficacy. Apart from inducing cancer cell redox imbalance, glucose inside cancer cells can also be consumed to synergize starvation therapy. Generating therapeutic gases such as NO, CO, and  $H_2$  through catalytic reactions is also an effective strategy for cancer treatment.

For traditional sonosensitizers, after electron–hole separation, they migrate to the sonosensitizer surface to come in contact with substrates and catalyze redox reactions. In comparison, piezoelectric sonosensitizers have higher electron–hole separation efficiencies under the piezoelectric effect induced by ultrasound. The band arrangement (valence and conduction band states) determines a piezoelectric catalyst's activity for specific chemical reactions, while the built-in electric field and piezoelectric potential can modulate the band structure and control internal charge carrier migration to the catalyst surface.<sup>34</sup> The accumulation of polarized surface charges attracts aggregation of valence band holes and conduction band electrons, inducing band tilting to increase redox potentials and effectively catalyze redox reactions.<sup>35</sup> The degree of band bending at the interface depends on the force of the internal electric field. By harnessing the piezoelectric potential to tune band bending and charge carrier transfer, the piezoelectric effect essentially modulates semiconductor charge transport behaviors. Varying degrees of band bending induced by adjusting the strength and direction of external stimulative strains lead to different surface charge carrier transfer kinetics, thus influencing reactions on the material's surface.

The crucial challenges limiting the efficacy of catalytic therapy are substrate restrictions and rapid electron–hole pair recombination. From a catalysis chemistry perspective, to



broaden substrate and therapeutic product scope, catalysts must possess sufficiently high VB and CB levels to provide adequate redox potentials. However, as the VB and CB levels increase, the band gap (the distance between the VB and CB) expands accordingly, which inevitably leads to poor catalytic activity and difficult electron-hole separation. Therefore, broadening the catalytic reaction scope and single catalyst catalytic activity are irreconcilable contradictions. The key question is how to simultaneously expand the energy absorption range, promote electron-hole separation, and avoid recombination to increase therapeutic product quantum yields.

Constructing heterojunction catalysts is thought to be a successful strategy to solve this problem.<sup>36</sup> The band positions and work functions of semiconductors are crucial indicators determining heterojunction electron transfer mechanisms, directly influencing their catalytic performance.<sup>37,38</sup> In Z-scheme heterojunction catalysts, the CB and VB of one semiconductor (catalyst I) are higher than those of the other semiconductor (catalyst II). Catalyst II has a higher work function than catalyst I. When the two catalysts make contact because of different Fermi levels, electrons move from catalyst I to catalyst II until the Fermi levels equilibrate. Hence, catalyst I's bands bend upward, while catalyst II's bands bend downward, providing a basis for hole combination in catalyst I's VB with electrons in catalyst II's CB through a tunneling effect. Meanwhile, the internal electric field generated from Fermi level equilibration can further facilitate the aforementioned combination of weaker redox potential electrons and holes while effectively suppressing the combination of high reduction potential electrons in catalyst I's CB and high oxidation potential holes in catalyst II's VB. Therefore, Z-scheme heterojunctions not only possess higher catalytic efficiency and longer carrier lifetimes but also have more extensive catalytic substrate scope.<sup>39-43</sup>

### 3 Sonocatalytic cancer therapy

Cancer has long been one of the most devastating illnesses. In comparison with other illnesses, its destructive disease progression and complex pathogenesis bring tremendous suffering to patients. For the treatment of cancer, a variety of therapies have been explored, with surgery, radiotherapy, chemotherapy, and immunotherapy being the most commonly used treatment modalities. Although these therapies have achieved clinical progress in cancer treatments, patients frequently suffer from short survival periods, poor quality of life, low cure rates, and severe side effects during treatment. In the mechanism of sonocatalytic therapy, sonosensitizers are key components for targeted tumoricidal oxidative damage. The active sites of sonosensitizers and the species and concentrations of therapeutically generated products are critical factors influencing sonocatalytic therapy. Therefore, tuning sonosensitizer structures and properties to maximize quantum yields and catalytic efficiencies under limited external stimu-

latory energy and substrate types and levels is vital for elevating the clinical potential of sonocatalytic cancer therapy.

#### 3.1 Traditional sonosensitizers

Sonocatalytic therapy can overcome the main drawback of inadequate penetration depth in photocatalysis. However, it is still extremely challenging to find sonosensitizers with excellent stability and high sonodynamic efficacy. Ultrasonic cavitation is the most important mechanism in sonocatalytic therapy, exciting sonosensitizers to undergo sonochemical reactions to produce therapeutic species. Liu *et al.* synthesized PMCS using ZIF-8 as a template *via* high-temperature calcination (Fig. 3a).<sup>44</sup> Due to its porous structure and large specific surface area, PMCS has great gas adsorption capabilities. This allows for the formation of more cavitation bubbles and lowers the cavitation threshold intensity by supplying more nucleation sites (Fig. 3b). Additionally, they captured the growth and collapse of cavitation bubbles and the generation of microjets under ultrasonic irradiation using a high-speed camera (Fig. 3c). Through electron spin resonance and dye measurements, the high levels of ROS produced by PMCs under ultrasound were confirmed, and this caused oxidative stress damage to cancer cells and efficient cancer suppression.

Most organic sonosensitizers originate from initial photosensitizers, whose potential skin sensitization and phototoxicity could also occur during sonocatalytic therapy. By easily functionalizing acenethiophenes with organoboron groups, Chen *et al.* proposed a novel approach to develop superior organic sensitizers (Fig. 3d).<sup>45</sup> The electron-deficient nature of the tris(aryl)boron groups in BTeTh led to decreased LUMO energy and narrowed band gaps. As a sonosensitizer, BTeTh-NPs displayed efficient  $\cdot\text{OH}$  generation under ultrasonic irradiation, as well as low cytotoxicity, avoiding potential skin phototoxicity issues during cancer treatment. Excellent biocompatibility and significant cancer suppression were observed from the *in vivo* therapeutic results of BTeTh-NPs (Fig. 3e). Boron functionalization of acenes reduces the phototoxicity of organic sonosensitizers, representing a promising strategy for sonocatalytic therapy. However, most organic sonosensitizers are severely hampered in sonocatalytic applications due to drawbacks such as poor water solubility, high phototoxicity, low sonotoxicity, and unfavorable pharmacokinetic properties.

Compared to organic materials, inorganic materials are considered potentially efficient sonosensitizers owing to their higher chemical stability and lower phototoxicity. The presence of ultrarich glutathione (GSH) inside tumors hampers ROS-based therapies, so enhancing sonocatalytic therapy by consuming GSH poses tremendous challenges. Yang *et al.* synthesized PtCu<sub>3</sub> nanocages *via* a one-pot solvothermal method.<sup>46</sup> In addition to serving as a novel sonosensitizer that generates ROS, including singlet oxygen ( $^1\text{O}_2$ ) and  $\cdot\text{OH}$ , when exposed to US radiation, PtCu<sub>3</sub> nanocages can also act as HRP-like nanozymes to catalyze H<sub>2</sub>O<sub>2</sub> decomposition into  $\cdot\text{OH}$  (Fig. 3f). Most importantly, PtCu<sub>3</sub> nanocages could serve as GSH-Px nanozymes to accelerate GSH consumption when oxi-

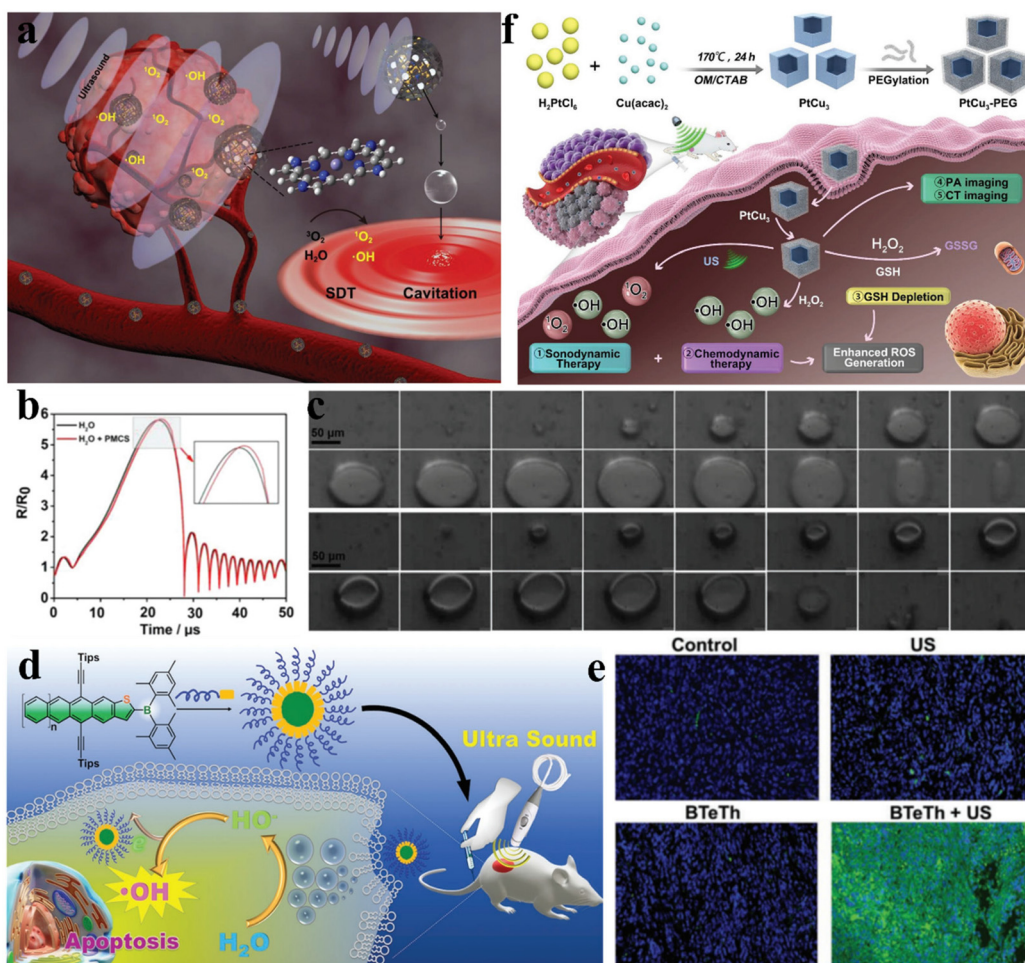


**Fig. 3** (a) Diagrammatic representation of PMCS-based sonodynamic cancer therapy. (b) The corresponding numerical simulation showing the variation in bubble deformation. (c) A high-speed camera captured the growth and collapse of cavitation bubbles as well as the formation of microjets in PMCS during US irradiation.<sup>44</sup> Copyright 2018, Wiley-VCH. (d) Diagrammatic representation of boron-doped acenethiophenes used for sonocatalytic therapy. (e) Fluorescence images of tumors collected from mice under different treatments.<sup>45</sup> Copyright 2022, Wiley-VCH. (f) Diagrammatic representation of PtCu<sub>3</sub> nanocage-based sonodynamic therapy enhanced by the GSH depletion strategy.<sup>46</sup> Copyright 2019, Wiley-VCH.

dizing molecules ( $\text{H}_2\text{O}_2$  and  $\text{O}_2$ ) are present. Studies conducted *in vitro* and *in vivo* demonstrated that owing to the robustly generated ROS and drastically decreased GSH, PtCu<sub>3</sub>-PEG nanocages enabled enhanced sonocatalytic therapy through CDT-potentiated sonodynamic therapy with delayed cancer growth.

In recent years, immunotherapy has made significant advances in cancer treatment. Notably, sonocatalytic therapy can efficaciously cause immunogenic cell death to provoke systemic antitumor immune responses.<sup>47</sup> Cheng *et al.* synthesized defective MoO<sub>x</sub> nanoparticles (NPs) *via* high-temperature pyrolysis.<sup>48</sup> The resultant MoO<sub>x</sub> under ultrasonication demonstrated highly effective ROS generation, elevating oxidative stress in tumors and eliciting ICD, thereby effectively suppressing cancer growth. More significantly, MoO<sub>x</sub> itself enhanced immune effects by stimulating DC maturation and activating the cGAS-STING pathway. Owing to the potent ICD caused by sonocatalytic therapy and efficient DC maturation

stimulated by MoO<sub>x</sub>, the combined therapy of MoO<sub>x</sub>-triggered sonocatalysis and aCTLA-4 further amplified the antitumor therapeutic effects, inhibiting cancer metastasis (Fig. 4a).

Challenges such as difficult *in vivo* gas delivery and random release leading to toxic side effects on normal tissues have always been the biggest obstacles hampering gas therapy. By integrating gas therapy with sonocatalytic therapy, controllable and precise generation of therapeutic gases can be achieved specifically at cancer sites. Ji *et al.* reported a 2D vermiculite nanosheet (VMT NS) loaded with L-arginine and polydopamine (Arg@VMT@PDA-PEG) that integrated NO-based gas therapy, 2D semiconductor sonocatalytic therapy, and Fenton reaction-based chemodynamic therapy for cancer treatment (Fig. 4b).<sup>5</sup> The catalytic mechanism is illustrated in Fig. 4c. Under ultrasonication, electron-hole separation occurs with electrons transferring to the CB of VMT NSs and holes remaining in the VB. Due to the high reduction potential of excited electrons in the CB,  $\text{O}_2^-$  can be generated *via* reduction reactions.

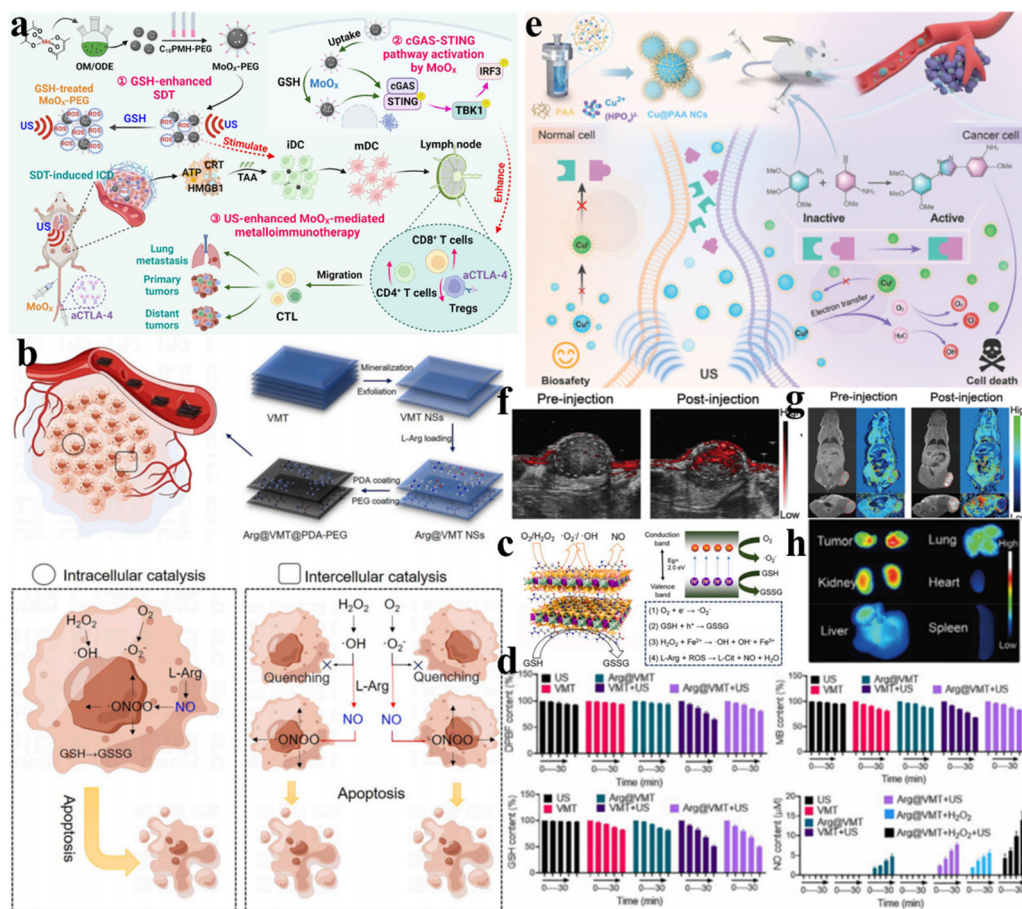


**Fig. 4** (a) MoO<sub>x</sub> nanosensitizers for cancer metalloimmunotherapy with ultrasound enhancement. Reproduced with permission.<sup>48</sup> Copyright 2023, Wiley-VCH. (b) Preparation and catalytic mechanism of Arg@VMT@PDA-PEG NSs. (c) Schematic illustration of the catalytic mechanism. (d) Catalytic performance of VMT-based nanocatalysts. (b–d) Reproduced with permission.<sup>5</sup> Copyright 2023, Elsevier Ltd. (e) Schematic diagram of the fabrication and mechanism of Cu@PAA NC-based sonodynamic therapy. (f) PA imaging and (g) T<sub>1</sub>-weighted MR imaging of Cu@PAA NCs. (h) Fluorescence imaging of the tumor and major organs collected from sacrificed mice after injection of Cu@PAA NCs. (e–h) Reproduced with permission.<sup>49</sup> Copyright 2022, Wiley-VCH.

Abundant Fe<sup>3+</sup>/Fe<sup>2+</sup> in VMT NSs mediated the Fenton reaction to effectively generate <sup>•</sup>OH and consume GSH. Additionally, ROS generated from ultrasound-triggered Arg@VMT@PDA-PEG could oxidize L-Arg into NO for synergistic gas therapy. <sup>•</sup>O<sub>2</sub><sup>-</sup>, <sup>•</sup>OH, GSSG, and NO generation was detected by DPBF, MB, DTNB, and DAF-2, respectively (Fig. 4d). A novel paradigm for cancer treatment was introduced, which combined three distinct catalytic processes.

Precise therapy can enable accurate diagnosis, delivery/bio-distribution monitoring, and treatment response to more efficiently achieve the ultimate goal of cancer elimination. Capitalizing on the precise spatiotemporal characteristics of ultrasound, Chen *et al.* designed and developed a multifunctional nanocatalytic platform based on ultrasmall poly(acrylic acid)-modified copper nanocomplexes (Cu@PAA NCs) that achieved site-specific activation of prodrugs and concurrently triggered bioorthogonal reactions to generate massive amounts of ROS (Fig. 4e).<sup>49</sup> In particular, Cu@PAA NCs demonstrated improved contrast in photoacoustic imaging

and magnetic resonance imaging (Fig. 4f and g). Moreover, the intrinsically benign biocompatibility of the renally clearable Cu@PAA NCs was shown (Fig. 4h). The development of imaging-guided sonocatalytic therapy systems using various imaging modalities can help achieve higher therapeutic efficacy by monitoring sonosensitizer administration and distribution in real time.

### 3.2 Piezoelectric sonosensitizers

Because ROS can concurrently damage numerous cellular components essential for biological processes, such as proteins, lipid membranes, and DNA, it is a very promising cancer treatment method for eliminating cancer cells. Ultrasound-induced mechanical vibrations lead to built-in electric fields on both sides of piezoelectric sonosensitizers, causing band shifts to increase redox potentials.<sup>50</sup> Few-layer black phosphorus (BP) nanosheets were utilized by Yang *et al.* to show that piezoelectric materials with appropriate energy band structures could produce ROS to induce apoptosis of cancer cells, making them



an effective catalyst for sonocatalytic cancer therapy.<sup>51</sup> As depicted in Fig. 5a, due to the piezoelectric effect, when ultrasound-induced mechanical vibrations are applied to BP nanosheets, the generated polarized charges migrate to the two sides of BP, establishing built-in electric fields and piezoelectric potentials that shift the band edges to increase redox potentials. In addition, specialized fluorescent probes identified the reactive oxygen species formed by BP under ultrasound as  $\cdot\text{OH}$  and  $\cdot\text{O}_2^-$  (Fig. 5b and c).

By leveraging efficient ROS generation, Shi *et al.* designed tetragonal  $\text{BaTiO}_3$  (T-BTO) to catalyze ROS generation, utilizing ultrasound-triggered catalytic actions to induce cytotoxicity for *in situ* cancer cell ablation.<sup>52</sup> Under ultrasonic vibration, the piezoelectric potential causes band bending, and the enormous energy from ultrasound separates electron-hole pairs, subsequently catalyzing ROS generation, including toxic  $\cdot\text{O}_2^-$  and  $\cdot\text{OH}$ , for cancer ablation. This method can dynamically control redox reactions and is more stable than traditional photodynamic therapy. *In vitro* and *in vivo* results confirmed that the T-BTO nanoparticles exerted remarkable cytotoxicity toward cancers under ultrasound while retaining high biocompatibility (Fig. 5d–g). Targeting the hypoxic tumor microenvironment, Liang *et al.* synthesized DSPE-PEG<sub>2000</sub>-coated ultrasmall barium titanate nanoparticles (P-BTOs) for ultrasound-triggered piezocatalytic and water splitting-based cancer therapy (Fig. 5h).<sup>53</sup> Under ultrasonication, strongly unbalanced

surface charges are created on ultrasmall P-BTO nanoparticles, triggering a cascade of redox reactions while concurrently generating ROS and  $\text{O}_2$ . The generated  $\text{O}_2$  significantly alleviated TME hypoxia by downregulating HIF-1 $\alpha$  expression, while the generated ROS effectively killed cancer cells.

Currently, piezoelectric sonosensitizers mainly utilize the band tilt effect to catalyze ROS generation for cancer cell ablation. Additionally, the high piezoelectric voltage produced by the piezoelectric effect can directly overcome the charge-induced band gap barrier to achieve electron-hole separation. Zhu *et al.* designed Mn-Ti bimetallic organic framework tetragonal nanosheets (MT-MOF TNS) capable of producing a high piezoelectric voltage that demonstrated remarkable antitumor efficacy (Fig. 6a). Moreover, the dielectric constant of MT-MOF nanosheets was found to be 2.9 V by piezoelectric force microscopy (PFM) when the electric field frequency was  $1 \times 10^4$  Hz, higher than the band gap of MT-MOF nanosheets (2.70 eV). They verified that the electron and hole separation was caused by the piezoelectric potential instead of sonoluminescence through the luminescence profiles and photoluminescence (PL) spectra of MT-MOF TNS (Fig. 6b and c).<sup>54</sup>

Apart from enhancing ROS generation by increasing charge separation, attenuating ROS consumption can also empower ROS to induce cancer cell apoptosis or necrosis.<sup>56</sup> Overexpressed GSH in the TME consumes sonosensitizer-generated ROS, thereby protecting cancer cells from oxidative

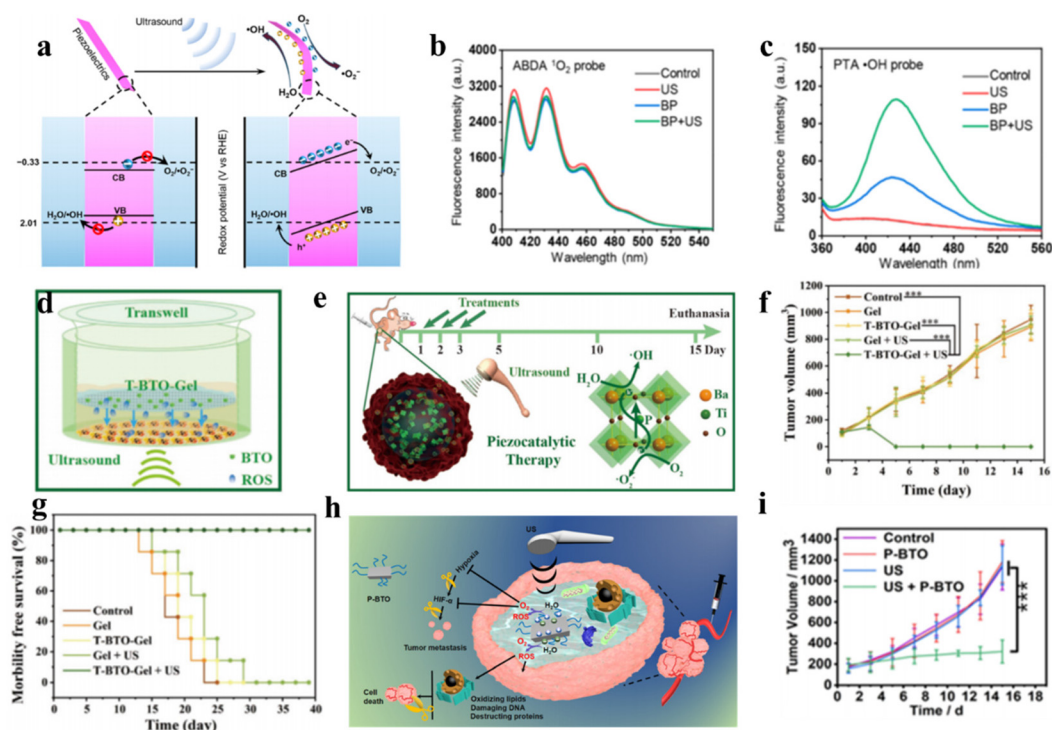


**Fig. 5** (a) Diagrammatic representation of the mechanism of piezoelectric polarization under ultrasound irradiation. The performance of  $\cdot\text{O}_2^-$  generation (b) and  $\cdot\text{OH}$  generation (c) under different conditions.<sup>51</sup> Copyright 2020, American Chemical Society. (d and e) Diagrammatic representation of the sonocatalytic cancer therapy of T-BTO *in vivo* and *in vitro*. Tumor growth curves (f) and survival curves (g) of 4T1 tumor-bearing mice after different treatments.<sup>52</sup> Copyright 2020, Wiley-VCH. (h) Diagrammatic representation of the mechanism of piezocatalytic therapy based on P-BTO. (i) Tumor growth curves under different treatments.<sup>53</sup> Copyright 2021, American Chemical Society.





**Fig. 6** (a) Diagrammatic representation of piezoelectric MT-MOF-mediated sonocatalytic therapy. (b) Luminescence profiles of MT-MOF TNS. (c) Photoluminescence (PL) spectra of MT-MOF TNS.<sup>54</sup> Copyright 2023, Wiley-VCH. (d) Diagrammatic representation of Bi<sub>2</sub>MoO<sub>6</sub> NPs for cancer therapy. Electron spin resonance (ESR) spectra of (e) <sup>•</sup>O<sub>2</sub><sup>-</sup> and <sup>1</sup>O<sub>2</sub> and (f) <sup>•</sup>OH. (g) Tumor growth curves under different treatments. (d–g) Reproduced with permission.<sup>55</sup> Copyright 2021, Wiley-VCH.

damage and limiting the clinical applications of sonocatalytic therapy. Dong *et al.* synthesized ultrathin 2D Bi<sub>2</sub>MoO<sub>6</sub> nanoribbons (BMO NRs) (Fig. 6d).<sup>55</sup> Cancer cell-engulfed BMO NRs consume endogenous GSH, disturbing the redox metabolic balance, while GSH-activated BMO NRs (GBMOs) possess oxygen vacancies that inhibit electron–hole recombination. This strengthens the efficacy of ROS generation in sonocatalytic therapy. Moreover, under ultrasonication, polarized GBMO NRs formed built-in electric fields that facilitated charge separation and suppressed recombination. Both *in vitro* and intracellular experiments demonstrated that GBMO could generate <sup>•</sup>O<sub>2</sub><sup>-</sup>, <sup>1</sup>O<sub>2</sub> and <sup>•</sup>OH (Fig. 6e and f). The antitumor efficacy of GBMO was validated in U14 tumor-bearing mice, where the

Bi<sub>2</sub>MoO<sub>6</sub> nanoribbon + US group achieved up to 96.6% tumor suppression (Fig. 6g).

### 3.3 Heterojunction sonosensitizers

For single catalysts, sufficiently high VB and CB levels are required to provide adequate redox potentials for broadening substrate and therapeutic product scope. However, as the VB and CB levels increase, the band gap expands accordingly, leading to difficult electron–hole separation and poor catalytic activity. Constructing heterojunctions has emerged as an effective solution to resolve this contradiction. In Z-scheme heterojunctions, the band arrangement is staggered, with the semiconductor possessing higher CB and VB levels (catalyst I)

and a higher Fermi level than the semiconductor with lower CB and VB levels (catalyst II). Under the built-in electric field, holes in the VB of catalyst I combine with electrons in the CB of catalyst II, leaving behind holes and electrons with stronger redox potentials in the VB of catalyst II and the CB of catalyst I, respectively. Z-scheme heterojunctions can accomplish effective catalytic reactions at high redox potentials, similar to how photosynthesis occurs in nature. Xue *et al.* anchored metal-free g-C<sub>3</sub>N<sub>4</sub> QDs on hollow mesoporous TiO<sub>2</sub> nanostructures to form TiO<sub>2</sub>@g-C<sub>3</sub>N<sub>4</sub> heterojunctions (Fig. 7a).<sup>57</sup> The Z-scheme charge migration markedly improved the separation/recombination kinetics of electron-hole pairs under ultrasonic stimulation, enhancing <sup>1</sup>O<sub>2</sub> and <sup>•</sup>OH yields, leading to redox homeostasis imbalance in cancer cells and triggering cancer cell apoptosis.

Additionally, Ji *et al.* synthesized FeOCl/FeOOH NS interfacial heterojunctions *via* a wet chemistry strategy based on alkali substitution reactions (Fig. 7c).<sup>58</sup> Due to differences in

work functions and Fermi levels, electron transfer occurred from FeOOH to FeOCl during hybridization, constructing a built-in electric field from FeOOH to FeOCl at their interface, which facilitated the building of the Z-scheme FeOCl/FeOOH heterojunction for effective charge carrier separation and promoted separation of holes and electrons to catalyze oxidation and reduction reactions. Fig. 7d illustrates how the built-in electric field in this FeOCl/FeOOH heterojunction-based system promoted Z-scheme charge transfer. The holes in the valence band of FeOCl possessed strong catalytic capabilities to split H<sub>2</sub>O to generate O<sub>2</sub>, while the generated O<sub>2</sub> was promptly reduced to H<sub>2</sub>O<sub>2</sub> by electrons in the conduction band of FeOOH. The self-supplied H<sub>2</sub>O<sub>2</sub> ensured efficient <sup>•</sup>OH generation through the FeOCl/FeOOH NS-catalyzed Fenton-like reaction, conferring excellent antitumor performance.

Ultrasound-induced mechanical vibrations lead piezoelectric materials to form internal electric fields, mediating efficient directional separation of excited electron-hole pairs.



**Fig. 7** (a) Schematic illustration of the synthetic procedure and catalytic mechanism of TCR-based cancer therapy.<sup>57</sup> Copyright 2023, Wiley-VCH. (b) Diagrammatic representation of the Z-scheme heterojunction FeOCl/FeOOH NSs for cancer treatment. (c) Preparation process of Z-scheme heterojunction FeOCl/FeOOH NSs. (d) Schematic illustration of the mechanism of the Z-scheme heterojunction for cancer therapy.<sup>58</sup> Copyright 2022, Springer Nature.



**Fig. 8** (a and b) Diagrammatic representation of the catalytic mechanism of NSH700 NSs.<sup>35</sup> Copyright 2021, Royal Society of Chemistry. (c) Diagrammatic representation of enhanced sonocatalytic therapy and CDT based on Cu<sub>2-x</sub>O-BTO NCs. (d) Diagrammatic representation of the catalytic mechanism of Cu<sub>2-x</sub>O-BTO NCs with a piezotronic effect.<sup>83</sup> Copyright 2022, American Chemical Society. (e) BiOCl/Bi<sub>2</sub>O<sub>3</sub> NS preparation with a Z-scheme heterojunction. (f) Mechanism of the Z-scheme heterojunction based on BiOCl/Bi<sub>2</sub>O<sub>3</sub> NSs. The performance of  $\cdot O_2^-$  generation (g) and CO generation (h) with US-excited electrons. GSH consumption (i) and  $\cdot OH$  generation (j) with US-excited holes.<sup>6</sup> Copyright 2022, American Association for the Advancement of Science.



Based on piezoelectric material heterojunctions, the redox potentials of excited electrons and holes are actively enhanced under mechanical stimulation from ultrasound. Based on piezoelectric photoelectrochemistry, Ji *et al.* prepared heterojunction-structured natural sphalerite nanosheets with piezoelectric photocatalytic effects (NSH700 NSs) *via* calcination and liquid exfoliation.<sup>35</sup> Fig. 8a and b show the separation and transfer of electron–hole pairs in NSH700 NS heterojunctions. From the perspective of needing stable excited holes and electrons, electrons tend to transfer to lower energy bands, meaning that holes and electrons in NSH700 NSs gather in the VB of ZnFe<sub>2</sub>O<sub>4</sub> and the CB of ZnO, respectively, through type I and type II transfer mechanisms. Under ultrasonic mechanical stress, polarized positive and negative charges are generated at the two ends of the ZnO and ZnS crystals, forming built-in electric fields across the crystals, constituting a novel mechanism for the separation and transfer of electron–hole pairs. In addition to enhancing electron–hole pair separation and transfer within ZnS, the positive and negative charges on the ZnS surface also served as driving forces for adjacent electrons and holes (ZnFe<sub>2</sub>O<sub>4</sub>). As a result, a specific number of holes in the VB of ZnFe<sub>2</sub>O<sub>4</sub> would transfer to the VB of ZnS, greatly increasing the oxidation potential. Similarly, electrons in the CB of ZnFe<sub>2</sub>O<sub>4</sub> transferred and accumulated in the VB of ZnO. The piezoelectric photocatalytic effect enabled excellent catalytic performance, demonstrating high-efficiency <sup>•</sup>O<sub>2</sub><sup>−</sup> and <sup>•</sup>OH generation as well as GSH consumption, whereupon the resultant intracellular oxidative burst caused apoptosis of cancer cells.

Additionally, Wang *et al.* synthesized Cu<sub>2−x</sub>O–BTO piezoelectric heterojunctions *via* a two-step hydrothermal and calcination method.<sup>83</sup> When Cu<sub>2−x</sub>O–BTO NCs were exposed to ultrasonic irradiation, the polarized electric field facilitated electron–hole separation and migration, causing band bending and shifting of the CB and VB to more favorable positions for catalyzing <sup>•</sup>O<sub>2</sub><sup>−</sup> and <sup>1</sup>O<sub>2</sub> generation (Fig. 8d). Moreover, owing to the existence of Cu(I) in the heterojunction structure, the Cu<sub>2−x</sub>O–BTO NCs also showed high Fenton activity to catalyze H<sub>2</sub>O<sub>2</sub> to produce <sup>•</sup>OH, directly killing cancer cells through CDT. Effective inhibition of 4T1 murine breast cancer was achieved *via* the synergistic combination of CDT and sonocatalytic therapy (Fig. 8c).

The critical factors restricting the effectiveness of catalytic therapy are the quick recombination of electron–hole pairs and the limitation of substrates. Ji *et al.* synthesized bulk layered bismuth oxychloride (BiOCl) *via* a hydrothermal approach and then selectively modified the edges of BiOCl and transformed them into Bi<sub>2</sub>O<sub>3</sub>, constructing a two-dimensional interplanar heterojunction (BiOCl/Bi<sub>2</sub>O<sub>3</sub>) (Fig. 8e).<sup>6</sup> The built-in electric field in the BiOCl/Bi<sub>2</sub>O<sub>3</sub> heterojunction facilitated Z-scheme charge transfer, as depicted in Fig. 8f. US irradiation concurrently induced the separation of electron–hole pairs in the VB of both BiOCl and Bi<sub>2</sub>O<sub>3</sub>, where the excited electrons crossed the band gap and moved to the CB of the catalyst while the holes remained in the VB. Then, under the direction of the built-in electric field, holes in the VB of BiOCl recom-

bined with electrons in the CB of Bi<sub>2</sub>O<sub>3</sub>, retaining electrons and holes with stronger redox potentials in the VB of Bi<sub>2</sub>O<sub>3</sub> and the CB of BiOCl, respectively. The two active catalytic sites located in the VB of Bi<sub>2</sub>O<sub>3</sub> and the CB of BiOCl could catalyze both traditional reactions such as O<sub>2</sub> + e<sup>−</sup> → <sup>•</sup>O<sub>2</sub><sup>−</sup> and GSH + h<sup>+</sup> → GSSG, as well as hard reactions such as CO<sub>2</sub> + 2H<sup>+</sup> + 2e<sup>−</sup> → CO + H<sub>2</sub>O and H<sub>2</sub>O + h<sup>+</sup> → <sup>•</sup>OH + H<sup>+</sup> (Fig. 8g–j). Built upon the two-dimensional interplanar Z-scheme heterojunction, prolonged electron and hole lifetimes and expanded catalytic reaction scope overcame TME restrictions on catalytic therapy, conferring outstanding antitumor efficacy. The preparation methods and properties of different types of sonosensitizers for sonocatalytic cancer therapy were summarized in Table 1.

## 4 Summary and outlook

Being a major global public health concern, cancer continues to be one of the main causes of human mortality.<sup>85</sup> According to the American Cancer Society's 2021 statistics, there were approximately 10 million cancer deaths and 19.3 million new cases of cancer worldwide in 2020.<sup>86</sup> Currently, people are adopting different types of cancer clinical treatment methods, including surgery, radiotherapy, chemotherapy, immunotherapy, and gene therapy. However, traditional therapies still exhibit some drawbacks. For instance, due to the strong metastatic potential and invasiveness of most malignant tumors, patients undergoing simple surgical resection still have a high probability of metastasis, necessitating supplementary radiotherapy or chemotherapy for complete cancer cell elimination. Owing to the high tissue penetrability of ionizing radiation, radiotherapy kills cancer cells while also damaging patients' normal cells.<sup>87</sup> After administration, chemotherapy drugs reach cancer sites through the blood circulation to take effect, but most lack targeting capabilities and have poor bio-availability, resulting in systemic toxicity. Gene therapy and immunotherapy are expensive and have limited universality.

Nanocatalytic therapy activates *in situ* tumor-localized catalytic reactions through nontoxic or low-toxicity nanocatalysts responding to specific intratumoral microenvironments or external stimuli, converting substrates in the tumor microenvironment into effective therapeutic agents to achieve tumor cell-specific oxidative damage and death without significantly affecting normal tissues. However, clinical applications of nanocatalytic therapy also face some challenges, such as the limited penetrability of external stimuli in biological bodies restricting energy absorption by *in vivo* catalysts, leading to insufficient catalytic dynamics, the low abundance of active sites on conventional catalyst surfaces, high recombination rates of excited electrons and holes resulting in severely compromised catalytic activity, and confined substrate types and levels in *in vivo* microenvironments directly affecting the species and concentrations of therapeutic products, thus reducing catalytic efficacy. Therefore, multidimensional modulation of nanocatalyst structures and properties to maximize quantum yields and catalytic efficiencies under limited exter-

**Table 1** Preparation method and properties of different types of sonosensitizers for sonocatalytic cancer therapy

Sonosensitizer types	Method	Materials	Properties	Ref.
Traditional sonosensitizers	Liquid phase exfoliation	Arg@VMT@PDA-PEG	Integrating SDT, CDT and gas therapy	5
		FePS <sub>3</sub> -PEG NSs	Combining SDT and CDT	59
		TiH <sub>1.924</sub>	Combining PTT and SDT	60
	Solvothermal method	PtCu <sub>3</sub> -PEG	CDT-enhanced SDT by depleting GSH	46
		D-MOF(Ti)	Synergistic SDT and CDT	61
		TPE-NN-Cu	Cu ion-augmented SDT	62
	Hydrothermal method	a-CoW-LDH nanosheets	Phase transformation-induced higher ROS generation	63
		Cu@PAA	Spatiotemporally ultrasound-mediated bioorthogonal catalysis	49
		Cu NDs	Ultrasound-responsive spatiotemporal CDT coupled with SDT	64
	Wrap-bake-strip method	Cu/TiO <sub>2</sub> -PEG	Synergistic CDT and SDT of TNBC	65
		Pyrolysis and etching	PMCS	High surface area and porosity and lower cavitation threshold
	High-temperature organic-phase method	TiS <sub>x</sub> NSS	Gas-enhanced SDT	66
	High-temperature decomposition procedure	MoO <sub>x</sub> -PEG	SDT-induced ICD effects	48
	Thermal decomposition method	TiO <sub>2</sub> @CaP	Ca <sup>2+</sup> ion overloading synergizes SDT	67
	Organic-phase synthesis strategy	PEBVO@PEG NRs	Photoetching approach inducing enriched oxygen vacancies	68
		MnVO <sub>3</sub>	Combining SDT and CDT	69
	Biom mineralization strategy	HClr nanoclusters	SDT-triggered ferroptosis-like cancer cell death	70
	O <sub>2</sub> -bubble bursting reaction	H <sub>x</sub> V <sub>2</sub> O <sub>5</sub>	Multivalent V element amplifies tumor oxidative stress	71
Solid-state mechanochemical method	WO <sub>x</sub> NBs	Defective structure enhanced SDT	72	
Molecular etching	PgP@Fe-COF	SDT and immune combination antitumor therapy	73	
Facile microwave-assisted polymerization	Mn-SCA	Nonthermal sonocavitation and SDT	74	
Piezoelectric sonosensitizers	Ultrasound exfoliation	BP nanosheets	Piezoelectric polarization causes band shifting	51
		T-BTO	First combination of piezocatalysis with cancer therapy	52
		UIO-66-Au NPs	Enhanced nanozyme catalytic therapy and piezoelectric SDT	75
	Hydrothermal method	P-BTO	Concurrent generation of O <sub>2</sub> and ROS	53
		BMO NRs	GSH-enhanced SDT	55
		Sv-MoS <sub>2</sub> NF	Introducing sulfur vacancies improves piezoelectricity	76
	Dynamic homogeneous reaction	BWO-Fe NSs	Enhanced SDT by doping metal ions	77
		BiOCl@PAA	Synergistic RCT and SDT	78
		SnS nanosheets	Piezoelectrocatalytic tumor immunoactivation	79
		Vv-r BiVO <sub>4</sub> NSs	Enhanced SDT by introducing cationic vacancy	80
		MT-MOF TNS	High sono-piezo voltage to directly excite charges	54
		MT-MOF TNS	High sono-piezo voltage to directly excite charges	54
Heterojunction sonosensitizers	Coupling calcination and liquid exfoliation	NSH700 NS	Piezo-photocatalytic cancer therapy	35
		FeOCl/FeOOH NSs	Highly efficient chemodynamic effect	58
	Hydrothermal method	BiOCl/Bi <sub>2</sub> O <sub>3</sub> NSs	Extending substrate selectivity	6
		TiO <sub>2</sub> @g-C <sub>3</sub> N <sub>4</sub>	Improved separation of electrons and holes	57
	Solvothermal method	COF@Co <sub>3</sub> O <sub>4</sub>	Synergistic nanocatalytic-sonodynamic cancer therapy	81
		COF@Co <sub>3</sub> O <sub>4</sub>	Synergistic nanocatalytic-sonodynamic cancer therapy	81
	Electrostatic attraction	Cu <sub>2-x</sub> O@TiO <sub>2-y</sub>	Enhanced CDT-SDT combination cancer therapy	82
Cu <sub>2-x</sub> O-BaTiO <sub>3</sub> NCs		Combining SDT and CDT	83	
Chemical deposition	Co <sub>3</sub> O <sub>4</sub> @TiO <sub>2-x</sub>	Improved spatial separation dynamics of electron-hole pairs	84	

nal stimulative energy and substrate types and concentrations is key to elevating the clinical potential of nanocatalytic therapies.

Compared to light, ultrasound has higher spatial precision, lower energy attenuation, and higher biological tissue penetrability, providing higher energy for catalysts. Meanwhile, due

to mechanisms such as sonoluminescence, most sonosensitizers initially used in sonocatalytic therapy originate from photosensitizers. Additionally, the mechanical vibrations induced by ultrasound lead to built-in electric fields on both sides of piezoelectric sonosensitizers, causing band shifts to increase redox potentials. Additionally, the piezoelectric poten-

tial generated *via* the piezoelectric effect can directly separate electrons and holes, improving electron–hole separation efficiencies and expanding substrate scope. Compared to single catalysts, constructing heterojunction sonosensitizers enables thorough electron–hole separation, reducing electron–hole recombination and enhancing catalytic efficiency. Z-scheme heterojunctions retain the strongest oxidation potential holes and strongest reduction potential electrons, expanding the substrate scope in the tumor microenvironment and increasing therapeutic product varieties.

Currently, sonocatalytic therapy is still in the early clinical evaluation stage and has not become part of standard cancer treatment regimens. Extensive research is still needed to bridge the gap between experimental applications and clinical practice. Several issues remain to be addressed for the clinical translation of sonocatalytic therapy. First, the sonosensitizer catalytic efficiency and biocompatibility were improved. Higher sonosensitizer doses may result in greater side effects; therefore, it is important to strike a balance between biocompatibility and therapeutic efficacy. Further research is required to enhance sonosensitizer catalytic efficiency, while clinical applications need to determine maximal tolerated doses, optimal ultrasound parameters, synergistic combinations with other therapies, *etc.* Additionally, biodegradable and metabolizable materials need to be developed. Second, the sonosensitizer-catalyzed reaction and application types should be expanded. Apart from the most common ROS generation, gas therapy has emerged as a novel antitumor treatment by achieving tumoricidal effects through specific accumulation of toxic gases at tumor sites. Catalysis-generated gaseous signaling molecules such as NO, CO, and H<sub>2</sub> have been demonstrated to play a part in disease treatment and physiological processes. Finally, translating basic research into clinical applications requires substantial time and monetary investments, necessitating more comprehensive clinical trials. Further exploration of the fundamental knowledge and clinical translation of nanosonosensitizer-based therapies will require collaborative efforts across disciplines from researchers, including engineers, chemists, physicists and biologists. We hope that advances in nanotechnology can spur more fundamental and technical breakthroughs to lay the foundation for unlimited future applications of nanosonosensitizer-based sonocatalytic therapies across various diseases.

## Conflicts of interest

The authors declare that they have no known competing financial interests or personal relationships that could have appeared to influence the work reported in this paper.

## Acknowledgements

This study was financially supported by a grant from the National Natural Science Foundation of China (Grant No.

32071322), National Natural Science Funds for Excellent Young Scholars (Grant No. 32122044), and Technology & Innovation Commission of Shenzhen Municipality (Grant No. JCYJ20210324113004010).

## References

- 1 B. Yang, Y. Chen and J. Shi, *Adv. Mater.*, 2019, **31**, e1901778.
- 2 H. Zhang, Z. Mao, Y. Kang, W. Zhang, L. Mei and X. Ji, *Coord. Chem. Rev.*, 2023, **475**, 214897.
- 3 X. Yuan, Y. Kang, J. Dong, R. Li, J. Ye, Y. Fan, J. Han, J. Yu, G. Ni, X. Ji and D. Ming, *Nat. Commun.*, 2023, **14**, 5140.
- 4 M. Ou, C. Lin, Y. Wang, Y. Lu, W. Wang, Z. Li, W. Zeng, X. Zeng, X. Ji and L. Mei, *J. Controlled Release*, 2022, **345**, 755–769.
- 5 Y. Nie, W. Chen, Y. Kang, X. Yuan, Y. Li, J. Zhou, W. Tao and X. Ji, *Biomaterials*, 2023, **295**, 122031.
- 6 L. Q. Chen, Z. Mao, Y. Wang, Y. Kang, Y. Wang, L. Mei and X. Y. Ji, *Sci. Adv.*, 2022, **8**, eabo7372.
- 7 M. Yuan, S. Liang, L. Yang, F. Li, B. Liu, C. Z. Yang, Z. Yang, Y. L. Bian, P. A. Ma, Z. Y. Cheng and J. Lin, *Adv. Mater.*, 2023, **35**, 2209589.
- 8 Y. Z. Zhou, T. Yang, K. Liang and R. Chandrawati, *Adv. Drug Delivery Rev.*, 2021, **171**, 199–214.
- 9 H. Lin, Y. Chen and J. L. Shi, *Chem. Soc. Rev.*, 2018, **47**, 1938–1958.
- 10 Y. Nie, W. Zhang, W. Xiao, W. Zeng, T. Chen, W. Huang, X. Wu, Y. Kang, J. Dong, W. Luo and X. Ji, *Biomaterials*, 2022, **289**, 121791.
- 11 X. Ji, L. Ge, C. Liu, Z. Tang, Y. Xiao, W. Chen, Z. Lei, W. Gao, S. Blake, D. De, B. Shi, X. Zeng, N. Kong, X. Zhang and W. Tao, *Nat. Commun.*, 2021, **12**, 1124.
- 12 L. Huang, J. Zhu, W. Xiong, J. Feng, J. Yang, X. Lu, Y. Lu, Q. Zhang, P. Yi, Y. Feng, S. Guo, X. Qiu, Y. Xu and Z. Shen, *ACS Nano*, 2023, **17**, 11492–11506.
- 13 D. W. Felsher, *Nat. Rev. Cancer*, 2003, **3**, 375–380.
- 14 T. J. Dougherty, G. B. Grindey, R. Fiel, K. R. Weishaupt and D. G. Boyle, *J. Natl. Cancer Inst.*, 1975, **55**, 115–121.
- 15 X. Li, S. Lee and J. Yoon, *Chem. Soc. Rev.*, 2018, **47**, 1174–1188.
- 16 Z. J. Zhou, J. B. Song, L. M. Nie and X. Y. Chen, *Chem. Soc. Rev.*, 2016, **45**, 6597–6626.
- 17 S. Yang, X. Wang, P. He, A. Xu, G. Wang, J. Duan, Y. Shi and G. Ding, *Small*, 2021, **17**, e2004867.
- 18 M. Yuan, S. Liang, L. Yang, F. Li, B. Liu, C. Yang, Z. Yang, Y. Bian, P. Ma, Z. Cheng and J. Lin, *Adv. Mater.*, 2023, **35**, e2209589.
- 19 W. Zeng, H. Zhang, X. Yuan, T. Chen, Z. Pei and X. Ji, *Adv. Drug Delivery Rev.*, 2022, **184**, 114241.
- 20 G. Canavese, A. Ancona, L. Racca, M. Canta, B. Dumontel, F. Barbaresco, T. Limongi and V. Cauda, *Chem. Eng. J.*, 2018, **340**, 155–172.
- 21 X. Lin, J. Song, X. Chen and H. Yang, *Angew. Chem., Int. Ed.*, 2020, **59**, 14212–14233.



- 22 D. Huang, J. Wang, C. Song and Y. Zhao, *Innovation*, 2023, **4**, 100421.
- 23 S. Liang, X. Deng, P. Ma, Z. Cheng and J. Lin, *Adv. Mater.*, 2020, **32**, e2003214.
- 24 X. Song, Q. Zhang, M. Chang, L. Ding, H. Huang, W. Feng, T. Xu and Y. Chen, *Adv. Mater.*, 2023, **35**, e2212259.
- 25 S. Umemura, N. Yumita, R. Nishigaki and K. Umemura, *Jpn. J. Cancer Res.*, 1990, **81**, 962–966.
- 26 J. Ouyang, Z. Tang, N. Farokhzad, N. Kong, N. Y. Kim, C. Feng, S. Blake, Y. Xiao, C. Liu, T. Xie and W. Tao, *Nano Today*, 2020, **35**, 100949.
- 27 Z. Jiang, W. Xiao and Q. Fu, *J. Controlled Release*, 2023, **361**, 547–567.
- 28 S. Son, J. H. Kim, X. Wang, C. Zhang, S. A. Yoon, J. Shin, A. Sharma, M. H. Lee, L. Cheng, J. Wu and J. S. Kim, *Chem. Soc. Rev.*, 2020, **49**, 3244–3261.
- 29 Y. Yang, J. Huang, M. Liu, Y. Qiu, Q. Chen, T. Zhao, Z. Xiao, Y. Yang, Y. Jiang, Q. Huang and K. Ai, *Adv. Sci.*, 2023, **10**, e2204365.
- 30 P. Curie and J. Curie, *Bull. Mineral.*, 1880, 90–93.
- 31 Y. Wang, P. Zang, D. Yang, R. Zhang, S. Gai and P. Yang, *Mater. Horiz.*, 2023, **10**, 1140–1184.
- 32 M. T. Chorsi, E. J. Curry, H. T. Chorsi, R. Das, J. Baroody, P. K. Purohit, H. Ilies and T. D. Nguyen, *Adv. Mater.*, 2019, **31**, 1802084.
- 33 X. Wang, X. Dai and Y. Chen, *Small*, 2023, **19**, e2301693.
- 34 S. Chen, P. Zhu, L. Mao, W. Wu, H. Lin, D. Xu, X. Lu and J. Shi, *Adv. Mater.*, 2023, e2208256.
- 35 Y. Kang, L. Lei, C. Zhu, H. Zhang, L. Mei and X. Ji, *Mater. Horiz.*, 2021, **8**, 2273–2285.
- 36 X. Y. Ji, Y. Kang, T. J. Fan, Q. Q. Xiong, S. P. Zhang, W. Tao and H. Zhang, *J. Mater. Chem. A*, 2020, **8**, 323–333.
- 37 H. L. Wang, L. S. Zhang, Z. G. Chen, J. Q. Hu, S. J. Li, Z. H. Wang, J. S. Liu and X. C. Wang, *Chem. Soc. Rev.*, 2014, **43**, 5234–5244.
- 38 C. Pan, Z. Mao, X. Yuan, H. Zhang, L. Mei and X. Ji, *Adv. Sci.*, 2022, **9**, e2105747.
- 39 C. Pan, M. Ou, Q. Cheng, Y. Zhou, Y. Yu, Z. Li, F. Zhang, D. Xia, L. Mei and X. Ji, *Adv. Funct. Mater.*, 2019, **30**, 1906466.
- 40 Y. Kang, Z. Li, Y. Yang, Z. Su, X. Ji and S. Zhang, *Healthc. Mater.*, 2021, **10**, e2001835.
- 41 X. Ji, Z. Tang, H. Liu, Y. Kang, L. Chen, J. Dong, W. Chen, N. Kong, W. Tao and T. Xie, *Adv. Mater.*, 2023, **35**, e2207391.
- 42 Y. Kang, Z. Li, F. Lu, Z. Su, X. Ji and S. Zhang, *Nanoscale*, 2022, **14**, 766–779.
- 43 M. Ou, C. Pan, Y. Yu, X. Wang, Y. Zhou, H. Zhang, Q. Cheng, M. Wu, X. Ji and L. Mei, *Chem. Eng. J.*, 2020, **390**, 124524.
- 44 X. Pan, L. Bai, H. Wang, Q. Wu, H. Wang, S. Liu, B. Xu, X. Shi and H. Liu, *Adv. Mater.*, 2018, **30**, e1800180.
- 45 K. Liu, Z. Jiang, F. Zhao, W. Wang, F. Jakle, N. Wang, X. Tang, X. Yin and P. Chen, *Adv. Mater.*, 2022, **34**, e2206594.
- 46 X. Zhong, X. Wang, L. Cheng, Y. a. Tang, G. Zhan, F. Gong, R. Zhang, J. Hu, Z. Liu and X. Yang, *Adv. Funct. Mater.*, 2019, **30**, 1907954.
- 47 S. Liang, J. Yao, D. Liu, L. Rao, X. Chen and Z. Wang, *Adv. Mater.*, 2023, **35**, e2211130.
- 48 Y. Wang, F. Gong, Z. Han, H. Lei, Y. Zhou, S. Cheng, X. Yang, T. Wang, L. Wang, N. Yang, Z. Liu and L. Cheng, *Angew. Chem., Int. Ed.*, 2023, **62**, e202215467.
- 49 L. Xia, M. Chen, C. Dong, F. Liu, H. Huang, W. Feng and Y. Chen, *Adv. Mater.*, 2023, **35**, e2209179.
- 50 X. Yuan, J. Shi, Y. Kang, J. Dong, Z. Pei and X. Ji, *Adv. Mater.*, 2023, e2308726.
- 51 Z. Li, T. Zhang, F. Fan, F. Gao, H. Ji and L. Yang, *J. Phys. Chem. Lett.*, 2020, **11**, 1228–1238.
- 52 P. Zhu, Y. Chen and J. Shi, *Adv. Mater.*, 2020, **32**, e2001976.
- 53 P. Wang, Q. Tang, L. Zhang, M. Xu, L. Sun, S. Sun, J. Zhang, S. Wang and X. Liang, *ACS Nano*, 2021, **15**, 11326–11340.
- 54 Q. Wang, Y. Tian, M. Yao, J. Fu, L. Wang and Y. Zhu, *Adv. Mater.*, 2023, e2301784.
- 55 Y. Dong, S. Dong, B. Liu, C. Yu, J. Liu, D. Yang, P. Yang and J. Lin, *Adv. Mater.*, 2021, **33**, e2106838.
- 56 Y. X. Xiong, C. Xiao, Z. F. Li and X. L. Yang, *Chem. Soc. Rev.*, 2021, **50**, 6013–6041.
- 57 M. He, H. Yu, Y. Zhao, J. Liu, Q. Dong, Z. Xu, Y. Kang and P. Xue, *Small*, 2023, **19**, e2300244.
- 58 Y. Kang, Z. Mao, Y. Wang, C. Pan, M. Ou, H. Zhang, W. Zeng and X. Ji, *Nat. Commun.*, 2022, **13**, 2425.
- 59 S. Lin, M. Yang, J. Chen, W. Feng, Y. Chen and Y. Zhu, *Small*, 2023, **19**, e2204992.
- 60 F. Gong, L. Cheng, N. Yang, Y. Gong, Y. Ni, S. Bai, X. Wang, M. Chen, Q. Chen and Z. Liu, *Nat. Commun.*, 2020, **11**, 3712.
- 61 S. Liang, X. Xiao, L. Bai, B. Liu, M. Yuan, P. Ma, M. Pang, Z. Cheng and J. Lin, *Adv. Mater.*, 2021, **33**, e2100333.
- 62 Y. Duan, Y. Yu, P. Liu, Y. Gao, X. Dai, L. Zhang, L. Chen and Y. Chen, *Angew. Chem., Int. Ed.*, 2023, **62**, e202302146.
- 63 T. Hu, W. Shen, F. Meng, S. Yang, S. Yu, H. Li, Q. Zhang, L. Gu, C. Tan and R. Liang, *Adv. Mater.*, 2023, **35**, e2209692.
- 64 W. Feng, Z. Liu, L. Xia, M. Chen, X. Dai, H. Huang, C. Dong, Y. He and Y. Chen, *Angew. Chem., Int. Ed.*, 2022, **61**, e202212021.
- 65 Q. Chen, M. Zhang, H. Huang, C. Dong, X. Dai, G. Feng, L. Lin, D. Sun, D. Yang, L. Xie, Y. Chen, J. Guo and X. Jing, *Adv. Sci.*, 2023, **10**, e2206244.
- 66 G. Li, H. Lei, Y. Yang, X. Zhong, F. Gong, Y. Gong, Y. Zhou, Y. Zhang, H. Shi, Z. Xiao, Z. Dong and L. Cheng, *Adv. Sci.*, 2022, **9**, e2201069.
- 67 X. Tan, J. Huang, Y. Wang, S. He, L. Jia, Y. Zhu, K. Pu, Y. Zhang and X. Yang, *Angew. Chem., Int. Ed.*, 2021, **60**, 14051–14059.
- 68 Z. Yang, M. Yuan, B. Liu, W. Zhang, A. Maleki, B. Guo, P. Ma, Z. Cheng and J. Lin, *Angew. Chem., Int. Ed.*, 2022, **61**, e202209484.
- 69 L. Sun, Y. Cao, W. Li, L. Wang, P. Ding, Z. Lu, F. Ma, Z. Wang and R. Pei, *Small*, 2023, **19**, e2300101.
- 70 T. Nie, W. Zou, Z. Meng, L. Wang, T. Ying, X. Cai, J. Wu, Y. Zheng and B. Hu, *Adv. Mater.*, 2022, **34**, e2206286.

- 71 L. Hou, F. Gong, Z. Han, Y. Wang, Y. Yang, S. Cheng, N. Yang, Z. Liu and L. Cheng, *Angew. Chem., Int. Ed.*, 2022, **61**, e202208849.
- 72 Y. Zhou, N. Yang, F. Gong, Y. Wang, X. Yang, Y. Dai, Q. Yu, L. Wang, W. Chen, M. Zhuo and L. Cheng, *ACS Nano*, 2022, **16**, 17242–17256.
- 73 D. Wang, L. Lin, T. Li, M. Meng, K. Hao, Z. Guo, J. Chen, H. Tian and X. Chen, *Adv. Mater.*, 2022, **34**, e2205924.
- 74 M. Liao, F. Chen, L. Chen, Z. Wu, J. Huang, H. Pang, C. Cheng, Z. Wu, L. Ma and Q. Lu, *Small*, 2023, e2302744.
- 75 L. Cai, J. Du, F. Han, T. Shi, H. Zhang, Y. Lu, S. Long, W. Sun, J. Fan and X. Peng, *ACS Nano*, 2023, **17**, 7901–7910.
- 76 Q. Wu, J. Zhang, X. Pan, Z. Huang, H. Zhang, J. Guo, Y. Xue, R. Shi and H. Liu, *Adv. Sci.*, 2023, e2301152.
- 77 Y. Ding, Y. Zhao, S. Yao, S. Wang, X. Wan, Q. Hu and L. Li, *Small*, 2023, **19**, e2300327.
- 78 Y. Liao, D. Wang, S. Zhu, R. Zhou, F. Rahbarizadeh and Z. Gu, *Nano Today*, 2022, **44**, 101510.
- 79 A. Wu, L. Jiang, C. Xia, Q. Xu, B. Zhou, Z. Jin, Q. He and J. Guo, *Adv. Sci.*, 2023, e2303016.
- 80 R. Zhao, H. Zhu, L. Feng, Y. Zhu, B. Liu, C. Yu, S. Gai and P. Yang, *Small*, 2023, e2301349.
- 81 C. Feng, J. Hu, C. Xiao, J. Yang, B. Xin, Z. Jia, S. Zhang, G. Tian, D. Zhang, L. Geng, L. Yan, L. Wang and B. Geng, *Chem. Eng. J.*, 2023, **460**, 141874.
- 82 B. Geng, S. Zhang, X. Yang, W. Shi, P. Li, D. Pan and L. Shen, *Chem. Eng. J.*, 2022, **435**, 134777.
- 83 Y. Zhao, S. Wang, Y. Ding, Z. Zhang, T. Huang, Y. Zhang, X. Wan, Z. L. Wang and L. Li, *ACS Nano*, 2022, **16**, 9304–9316.
- 84 S. Zhang, L. Zhang, J. Hu, X. He, B. Geng, D. Pan and L. Shen, *Chem. Eng. J.*, 2023, **458**, 141485.
- 85 R. L. Siegel, K. D. Miller, N. S. Wagle and A. Jemal, *CA Cancer J. Clin.*, 2023, **73**, 17–48.
- 86 H. Sung, J. Ferlay, R. L. Siegel, M. Laversanne, I. Soerjomataram, A. Jemal and F. Bray, *CA-Cancer J. Clin.*, 2021, **71**, 209–249.
- 87 M. R. Gill and K. A. Vallis, *Chem. Soc. Rev.*, 2019, **48**, 540–557.